J Eng Math (2007) 59:229–238
DOI 10.1007/s10665-007-9140-z

Modeling study of migration-driven lateral instability in autocatalytic systems

Zsanett Virányi · Ágota Tóth · Dezső Horváth

Received: 13 February 2006 / Accepted: 31 January 2007 / Published online: 20 March 2007

Abstract The lateral stability of reaction fronts in simple autocatalytic models with the components carrying various charges is investigated when the system is exposed to an inhomogeneous electric field parallel to the direction of propagation. The enhanced migrational flux of the reactant destabilizes the planar front giving rise to a cellular structure because the electric field strength is greater on the reactant side of the reaction front. The onset of instability depends not only on the charge difference between the reactant and the autocatalyst but also on the variation of specific conductance in the course of the reaction, which results in a difference in electric field strength on the opposite sides of the reaction front.

Keywords Autocatalytic reaction front · Lateral instability · Migration-driven instability

1 Introduction

In autocatalysis the positive feedback results from the chemical nature of one of the products as it increases the rate of its own production. From the interaction between autocatalytic reactions and transport processes a chemical front may arise, which can be characterized by the distribution of concentrations and the velocity of propagation [1,2]. The reaction front, which spatially separates the unreacted chemicals from the products, is the thin interface where the autocatalytic reaction takes place at a significant rate. It generally retains the symmetry of the local initiation in a homogeneous reactant mixture in the absence of convection; however, under certain conditions concentration gradients transverse to the direction of propagation may arise leading to the formation of a cellular pattern from the ever-present microscopic noise [3,4]. This phenomenon is called the lateral instability of reaction fronts.

Theoretical studies have shown that planar reaction–diffusion fronts may lose stability when the diffusion of the reactant is dominant over that of the autocatalyst through the reaction zone [5–8]. It has also been shown that a strong feedback is necessary; in single-step quadratic autocatalysis planar fronts remain stable. In aqueous solutions the diffusion coefficients of components are hardly tunable, which is why the selective slowing down of the autocatalyst is achieved in experimental systems by binding it into an immobile species [9–12]. The reversible binding decreases the concentration of the free autocatalyst behind the

Z. Virányi · Á. Tóth · D. Horváth (✉)
Department of Physical Chemistry, University of Szeged, P.O. Box 105, Szeged 6701, Hungary
e-mail: horvathd@chem.u-szeged.hu

Table 1 Investigated models

	Reaction model	Reaction rate	$z_B - z_A$
1	$A^- \rightarrow B + C^+ + D^{2-}$	$k_c c_A c_B^2$	1
2	$A^- \rightarrow B^+ + C^{2-}$	$k_c c_A c_B^2$	2
3	$A^- \rightarrow B^{2+} + C^{2-} + D^-$	$k_c c_A c_B^2$	3
4	$A^- \rightarrow B^- + C^+ + D^-$	$k_c c_A c_B^2$	0
5	$A^- \rightarrow B^+ + C^{2-}$	$k_q c_A c_B$	2

front and hence its flux across the reaction zone [13]. The same effect may be observed if the autocatalyst slowly decays following its production by forming an inert product [14].

In our experimental studies the autocatalytic chlorite ion oxidation of tetrathionate ion has been in focus, where a constant external electric field parallel to the direction of propagation either enhances the mixing of the reacting species or tends to separate them via the arising ionic migration depending on the orientation of the field [15–17]. In the latter scenario less autocatalyst is produced in the reaction leading to a further decrease in its concentration gradient across the reaction zone; hence cellular fronts may be observed at a smaller binding than in the absence of an electric field. If the reaction front is exposed to an inhomogeneous electric field, i.e., no conducting salt is added to the mixture, the electric field strength will be greater ahead of the reaction front because the specific conductance of the solution increases in the course of the chlorite–tetrathionate reaction [18]. Planar fronts now lose stability when the field orientation induces migration towards the reaction zone increasing the concentration gradient of the autocatalyst with respect to that of the reactant; lateral instability therefore arises, even though diffusion itself would stabilize the planar symmetry. We have shown theoretically and experimentally that in the chlorite–tetrathionate reaction it is the enhanced migrational flux of the reactants with respect to that of the autocatalyst that drives the instability due to the greater electric field residing ahead of the reaction front [19].

In this work we investigate the stability of reaction fronts existing in prototype models of simple autocatalytic systems. We place various charges on the reacting species and include inert ionic products to account for the increase in specific conductance in the reaction. In the constructed reaction–diffusion-migration systems we find the planar-front solutions upon varying the external electric field applied parallel to the direction of propagation. We then investigate the stability of the one-dimensional solutions to transverse perturbations by carrying out a linear stability analysis. By locating the onset of lateral instability and comparing the results of the various models, we will identify the key parameters that characterize the migration-driven instability arising in these systems.

2 Reaction–diffusion-migration model

We have investigated the lateral stability of reaction fronts in cubic autocatalysis with various charges on the species (models 1–4 in Table 1) and in quadratic autocatalysis (model 5 in Table 1), when the two-dimensional systems are exposed to an external electric field parallel to the direction of propagation. In all systems the reactant anion A^- is converted into the autocatalyst B, where the byproducts C and D ensure the increase of conductivity in the course of the reaction. A positively charged inert counter ion is also present in the system to account for the charge balance.

These reaction models in the electric field are described mathematically with a general balance equation in the from of

$$\frac{\partial C_i}{\partial t} = D_i \nabla^2 C_i + \frac{z_i F D_i}{RT} \nabla \left(C_i \nabla \Psi \right) + \nu_i R, \tag{1}$$

where C_i is the concentration and z_i is the charge of the ith component having a diffusion coefficient D_i and a stoichiometric coefficient ν_i, R is the local rate of reaction and Ψ represents the electric potential.

The first term on the right-hand side of Eq. 1 describes diffusion, the second expresses the migration in an inhomogeneous electric field and the third arises from the kinetics of the chemical reaction.

To characterize the systems completely, we must consider the charge balance

$$\frac{\partial Q}{\partial t} = \sum_{i=1}^{n} \left(z_i F D_i \nabla^2 C_i + \frac{z_i^2 F^2 D_i}{RT} \nabla \left(C_i \nabla \Psi \right) \right) = 0, \tag{2}$$

where the number of species $n = 4-5$ depending on the model. In Eq. 2 we also state that no macroscopic charge separation occurs in the models, i.e., $Q = 0$, which is the general case for a real chemical-system run in an aqueous solution.

Upon the introduction of dimensionless parameters, Eqs. 1 and 2 lead to

$$\frac{\partial c_i}{\partial \tau} = \delta_i \nabla^2 c_i + z_i \delta_i \nabla \left(c_i \nabla \psi \right) + \nu_i r, \tag{3}$$

$$0 = \sum_{i=1}^{n} \left(z_i \delta_i \nabla^2 c_i + z_i^2 \delta_i \nabla \left(c_i \nabla \psi \right) \right), \tag{4}$$

where the dimensionless concentration $c_i = C_i / C_{1,0}$ is scaled to the initial concentration of the reactant A far ahead of the front, $\delta_i = D_i / D_1$ represents the relative diffusivity and the dimensionless potential is given as $\psi = \Psi F / (RT)$. For cubic autocatalysis (models 1–4 in Table 1) the reaction rate $r = c_1 c_2^2$, the dimensionless time scale $\tau = k_c C_{1,0}^2 t$ and dimensionless length scales $\xi = x\sqrt{k_c C_{1,0}^2 / D_1}$, $\eta = y\sqrt{k_c C_{1,0}^2 / D_1}$. For quadratic autocatalysis (model 5 in Table 1) $r = c_1 c_2$, the dimensionless time scale $\tau = k_q C_{1,0} t$ and dimensionless length scales $\xi = x\sqrt{k_q C_{1,0} / D_1}$, $\eta = y\sqrt{k_q C_{1,0} / D_1}$, redefining ∇ as $(\partial/\partial\xi, \partial/\partial\eta)^T$.

In the spatially extended system we orient the ξ-axis in the direction of propagation and define boundary conditions that are realistic for experimental setups. Far ahead and behind the front, i.e., as $|\xi| \to \infty$, the concentration gradients vanish, which does not mean that the flux tends to zero because of the ionic migration under the electric field. The potential gradient at the limits is driven by the constant current density J, where ξ corresponds to the direction of the front propagation

$$\left. \frac{\partial \psi}{\partial \xi} \right|_{\pm\infty} = \frac{-j}{\sum_{i=1}^{n} z_i^2 \delta_i c_{i,\pm\infty}}, \tag{5}$$

where the dimensionless current density is given as $j = J / (F\sqrt{k_c C_{1,0}^4 D_1})$ for cubic autocatalysis (models 1–4 in Table 1) and $j = J / (F\sqrt{k_q C_{1,0}^3 D_1})$ for quadratic autocatalysis (model 5 in Table 1), and the denominator is essentially the specific conductance at the appropriate boundary ($\kappa_{\pm\infty}$). The concentrations are also given at $\xi \to$ as $c_1 = c_n = 1$ and $c_2 = \cdots = c_{n-1} = 0$, corresponding to the initial reactant solution containing only A and the inert counter ion.

The two-dimensional system in Eqs. 3 and 4 has been solved on a rectangular grid of 201×401 points with spacing $h = 0.5$ using the standard nine-point formula for the Laplacian and an explicit Euler method with $\Delta\tau = 10^{-3}$. Following an iteration step for Eq. 3, the potential field has been updated by applying a relaxation method to Eq. 4. For initial conditions, a local perturbation of the planar front is introduced by randomly displacing the rows by one grid unit in the direction of propagation. During the integrations the entire grid is continuously shifted forward to keep the reaction front centered in the grid.

3 Planar reaction front solution

Upon solving for planar fronts all gradients in the η-direction disappear, so Eqs. 3 and 4 describe a one-dimensional problem. We may introduce a traveling coordinate $\zeta = \xi - u\tau$, where u is the velocity of front

propagation, and hence transform Eqs. 3 and 4 into ordinary differential equations as

$$0 = \delta_i \frac{\mathrm{d}^2 c_i}{\mathrm{d}\zeta^2} + u\frac{\mathrm{d}c_i}{\mathrm{d}\zeta} + z_i\delta_i\left(\frac{\mathrm{d}c_i}{\mathrm{d}\zeta}\frac{\mathrm{d}\psi}{\mathrm{d}\zeta} + c_i\frac{\mathrm{d}^2\psi}{\mathrm{d}\zeta^2}\right) + \nu_i r, \tag{6}$$

$$0 = \sum_{i=1}^{n}\left[z_i\delta_i\frac{\mathrm{d}^2 c_i}{\mathrm{d}\zeta^2} + z_i^2\delta_i\left(\frac{\mathrm{d}c_i}{\mathrm{d}\zeta}\frac{\mathrm{d}\psi}{\mathrm{d}\zeta} + c_i\frac{\mathrm{d}^2\psi}{\mathrm{d}\zeta^2}\right)\right]. \tag{7}$$

The concentrations far behind the front, i.e., as $\zeta \to -\infty$, can be obtained from the integral of Eq. 6

$$0 = \left[\delta_i\frac{\mathrm{d}c_i}{\mathrm{d}\zeta}\right]_{-\infty}^{+\infty} + [uc_i]_{-\infty}^{+\infty} + \left[z_i\delta_i c_i\frac{\mathrm{d}\psi}{\mathrm{d}\zeta}\right]_{-\infty}^{+\infty} + \nu_i\int_{-\infty}^{+\infty} r\,\mathrm{d}\zeta, \tag{8}$$

in which the first term vanishes for each i. Since the reactant is consumed in the course of the reaction, $c_1 = 0$ at $\zeta = -\infty$, yielding an expression for the integral of the reaction rate from Eq. 8 for $i = 1$ as

$$\int_{-\infty}^{+\infty} r\,\mathrm{d}\zeta = -\frac{1}{\nu_1}\left(u - z_1\delta_1\left.\frac{\mathrm{d}\psi}{\mathrm{d}\zeta}\right|_{+\infty}\right) = u - \left.\frac{\mathrm{d}\psi}{\mathrm{d}\zeta}\right|_{+\infty}. \tag{9}$$

The substitution of Eq. 9 in Eq. 8 for $i = 2, \ldots, n-1$ results in a set of nonlinear equations for $c_2, \ldots, c_{n-1}$ at $\zeta = -\infty$, which can readily be solved for a given j and u. The concentration of the counter ion at the limit is then obtained from the charge balance

$$c_n = -\frac{1}{z_n}\sum_{i=1}^{n-1} z_i c_i. \tag{10}$$

The functional form of the concentration profiles close to the limits $|\zeta| \to \infty$ can be determined by investigating Eq. 6 in the phase space $(c_1, \ldots, c_{n-1}, v_1, \ldots, v_{n-1})$, where the new variables are defined as $v_i = \mathrm{d}c_i/\mathrm{d}\zeta$. The boundary conditions of Eq. 6 appear as steady states in the phase space and the concentration profiles as the heteroclinic orbit connecting them. The governing equations comprise the definition of the new variables and the rearranged Eq. 6 with the potential gradient given from

$$j = -\sum_{i=1}^{n}\left(z_i\delta_i\frac{\mathrm{d}c_i}{\mathrm{d}\zeta} + z_i^2\delta_i c_i\frac{\mathrm{d}\psi}{\mathrm{d}\zeta}\right), \tag{11}$$

an integral of Eq. 6, since the latter is essentially $0 = -\mathrm{d}j/\mathrm{d}\zeta$. The concentration of the counter ion c_n is eliminated by applying the charge balance via Eq. 10.

The linear stability analysis at the steady state corresponding to $\zeta = -\infty$ yields a single physically acceptable positive eigenvalue; hence the trajectory is approximated as

$$\begin{pmatrix} c_1 \\ \vdots \\ c_{n-1} \end{pmatrix} = \begin{pmatrix} 0 \\ \vdots \\ c_{n-1,-\infty} \end{pmatrix} + \mathbf{e}_+\,\mathrm{e}^{\lambda_+\zeta}, \tag{12}$$

where λ_+ is the positive eigenvalue and $\mathbf{e}_+$ is the eigenvector associated with it.

There are $(n-1)$ negative eigenvalues at the steady state representing $\zeta = \infty$; hence the trajectory may be formulated as

$$\begin{pmatrix} c_1 \\ \vdots \\ c_{n-1} \end{pmatrix} = \begin{pmatrix} 1 \\ \vdots \\ 0 \end{pmatrix} + \sum_{i=1}^{n-1}\mathcal{C}_i\,\mathbf{e}_{-,i}\,\mathrm{e}^{\lambda_{-,i}\zeta}, \tag{13}$$

where $\lambda_{-,i}$ is the negative eigenvalue and $\mathbf{e}_{-,i}$ is the appropriate eigenvector.

Equations 6 and 7 are solved by a relaxation method on an equally spaced grid with 501–701 points depending on the model with grid spacing $h = 0.1$. For the discretization we have used the forward difference formula for the first derivative in the second term of Eq. 6 and the centered difference for the rest and the standard three-point formula for the Laplacian to obtain

$$\frac{\mathrm{d}c_{i,j}}{\mathrm{d}\tau} = \delta_i \frac{c_{i,j+1} - 2c_{i,j} + c_{i,j-1}}{h^2} + u\frac{c_{i,j+1} - c_{i,j}}{2h} + z_i\delta_i\left(\frac{(c_{i,j+1} - c_{i,j-1})(\psi_{j+1} - \psi_{j-1})}{4h^2} + \bar{c}_{i,j}\frac{\psi_{j+1} - 2\psi_j + \psi_{j-1}}{h^2}\right) + \nu_i r_j \tag{14}$$

$$0 = \sum_{i=1}^{n} z_i\delta_i \frac{c_{i,j+1} - 2c_{i,j} + c_{i,j-1}}{h^2} + \sum_{i=1}^{n} z_i^2\delta_i\left(\frac{(c_{i,j+1} - c_{i,j-1})(\psi_{j+1} - \psi_{j-1})}{4h^2} + \bar{c}_{i,j}\frac{\psi_{j+1} - 2\psi_j + \psi_{j-1}}{h^2}\right) \tag{15}$$

for the jth grid point, where $\bar{c}_{i,j} = (c_{i,j+1} + c_{i,j-1} + 2c_{i,j})/4$ is introduced for improved numerical stability. The boundary condition on the left is taken from Eq. 12 resulting in

$$\left(\frac{\mathrm{d}c_i}{\mathrm{d}\zeta}\right)_j = \lambda_+ (c_{i,j} - c_{i,-\infty}), \tag{16}$$

while that on the right is derived from Eq. 13 leading to

$$\begin{pmatrix} \frac{\mathrm{d}c_1}{\mathrm{d}\zeta} \\ \vdots \\ \frac{\mathrm{d}c_n}{\mathrm{d}\zeta} \end{pmatrix}_j = \mathbf{M}\begin{pmatrix} c_{1,j} \\ \vdots \\ c_{n-1,j} \end{pmatrix} - \mathbf{v}, \tag{17}$$

where $\mathbf{M}$ is an n by $(n-1)$ matrix with the last row being a linear combination of the rest due to the charge balance. The matrix $\mathbf{M}$ and the vector $\mathbf{v}$ contain the eigenvalues and the components of the eigenvectors from Eq. 13. The boundary condition for the discretized potential is then obtained by substituting Eqs. 16 and 17, respectively, in Eq. 11.

Equation 15 with the boundary conditions represents a homogeneous set of linear equations for ψ_j with a tridiagonal matrix that can be easily solved for a given set of concentration values provided $\phi_0 = 0$. The ODE in Eq. 6 with the boundary conditions is then solved with the CVODE package [20] to reach the time-independent solution, i.e., $\mathrm{d}c_{i,j}/\mathrm{d}\tau \to 0$. During the integration the velocity of front propagation and the concentration at $\zeta = -\infty$ are regularly adjusted according to Eq. 9 to a value for velocity within a preset error of 10^{-7}.

4 Linear stability analysis

On determining the stability of planar reaction fronts, we introduce a small spatial perturbation transverse to the direction of propagation, hence the front position becomes $\zeta_p(\eta, \tau) = \sum_k \Phi_k(\eta, \tau)$, where k is the wavenumber associated with the perturbation. The concentration and the potential field can therefore be written as

$$c_i(\zeta, \eta, \tau) = c_{i,0}(\zeta) + \sum_{k=1}^{\infty} c_{i,1,k}(\zeta)\Phi_k(\eta, \tau) = c_{i,0}(\zeta) + \sum_{k=1}^{\infty} c_{i,1,k}(\zeta)\mathrm{e}^{\omega\tau + ik\eta}, \tag{18}$$

$$\psi(\zeta, \eta, \tau) = \psi_0(\zeta) + \sum_{k=1}^{\infty} \psi_{1,k}(\zeta)\Phi_k(\eta, \tau) = \psi_0(\zeta) + \sum_{k=1}^{\infty} \psi_{1,k}(\zeta)\mathrm{e}^{\omega\tau + ik\eta}, \tag{19}$$

where $c_{i,0}$ and $\psi_{i,0}$ represent the planar front, i.e., the solution of Eqs. 6 and 7. The perturbation is localized to the reaction front, where r is significant; therefore we require that $c_{i,1,k} \to 0$ and $\psi_{1,k} \to 0$ as $|\zeta| \to \infty$. In the linear stability analysis having substituted Eqs. 18 and 19 in Eqs. 3 and 4 in the traveling-coordinate system, we only consider first-order perturbations; the spatial modes then decouple and we obtain

$$\omega c_{i,1,k} = \delta_i \frac{\mathrm{d}^2 c_{i,1,k}}{\mathrm{d}\zeta^2} + u\frac{\mathrm{d}c_{i,1,k}}{\mathrm{d}\zeta} + z_i\delta_i\left(\frac{\mathrm{d}c_{i,0}}{\mathrm{d}\zeta}\frac{\mathrm{d}\psi_{1,k}}{\mathrm{d}\zeta} + \frac{\mathrm{d}c_{i,1,k}}{\mathrm{d}\zeta}\frac{\mathrm{d}\psi_0}{\mathrm{d}\zeta} + c_{i,1,k}\frac{\mathrm{d}^2\psi_0}{\mathrm{d}\zeta^2} + c_{i,0}\frac{\mathrm{d}^2\psi_{1,k}}{\mathrm{d}\zeta^2} - k^2 c_{i,0}\psi_{1,k}\right) - \delta_i k^2 c_{i,1,k} + \nu_i J_k, \tag{20}$$

$$0 = \sum_{i=1}^{n}\left[z_i\delta_i\left(\frac{\mathrm{d}^2 c_{i,1,k}}{\mathrm{d}\zeta^2} - k^2 c_{i,1,k}\right) + z_i^2\delta_i\left(\frac{\mathrm{d}c_{i,0}}{\mathrm{d}\zeta}\frac{\mathrm{d}\psi_{1,k}}{\mathrm{d}\zeta} + \frac{\mathrm{d}c_{i,1,k}}{\mathrm{d}\zeta}\frac{\mathrm{d}\psi_0}{\mathrm{d}\zeta} + c_{i,1,k}\frac{\mathrm{d}^2\psi_0}{\mathrm{d}\zeta^2} + c_{i,0}\frac{\mathrm{d}^2\psi_{1,k}}{\mathrm{d}\zeta^2} - k^2 c_{i,0}\psi_{1,k}\right)\right] \tag{21}$$

for the terms first order with respect to Φ_k, where $J_k = \sum_{i=1}(\partial r/\partial c_i)_0\, c_{i,1,k}$, and ω represents the temporal eigenvalue. In case $\omega > 0$ for some value of k, the perturbation grows exponentially in time, identifying an unstable planar front. Equations 20 and 21 may be rewritten in matrix form as

$$\omega \begin{pmatrix} 1 \ldots 0\ 0 \\ \vdots \ddots \vdots\ \vdots \\ 0 \ldots 1\ 0 \\ 0 \ldots 0\ 0 \end{pmatrix} \begin{pmatrix} c_{1,1,k} \\ \vdots \\ c_{n,1,k} \\ \psi_{1,k} \end{pmatrix} = \widehat{\mathbf{M}} \begin{pmatrix} c_{1,1,k} \\ \vdots \\ c_{n,1,k} \\ \psi_{1,k} \end{pmatrix}, \tag{22}$$

where the matrix operator $\widehat{\mathbf{M}}$ only depends on $c_{i,0}$, ψ_0, and k.

For the calculation of the eigenvalue ω, Eqs. 20 and 21 are first discretized in the same fashion as Eqs. 6 and 7, which transforms $\widehat{\mathbf{M}}$ into a regular banded matrix with a bandwidth of $2n+1$. The generalized eigensystem itself has then been solved with the DGGEV routine from the LAPACK package [21] to find the eigenvalues, among which the one with the largest real part determines the stability of the solution with respect to the selected spatial mode. For a given planar front the procedure is repeated to construct the dispersion curve $\omega = \mathcal{F}(k)$ by plotting the appropriate distinct eigenvalue as a function of the spatial wavenumber.

We take equal diffusivities for all components, i.e., $\delta_i = 1$, in which case the systems are diffusionally stable.

5 Results and discussion

In the absence of an external electric field, i.e., $j = 0$, the investigated models support a reaction front with constant velocity of propagation, which is represented with stationary concentration profiles in the moving-coordinate system. While the concentrations ahead of the fronts are defined by the initial state and hence are independent of the electric field, the concentration of the products behind the front varies with the strength of the applied external field. Figure 1 shows the concentration profiles developed for model 1 in Table 1 in a positive electric field ($j = 0.6$). The negatively charged reactants migrate backward into the reactant zone, locally enhancing the rate of reaction which leads to a greater autocatalyst build-up behind the front: the final concentration of B increases to 1.33 from 1 observed in the absence of electric field. The inert products of the reaction have different charges so that their concentrations are no longer the same as that of the autocatalyst. The positively charged C migrates forward and therefore reaches an even greater

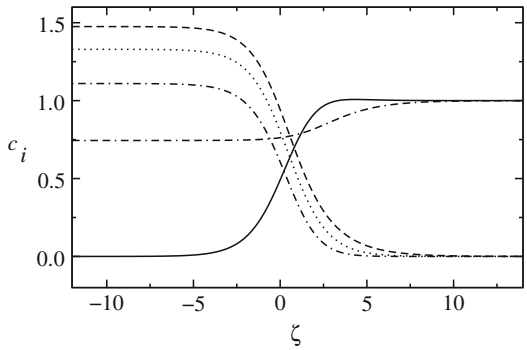

Fig. 1 Concentration profiles for model 1 in Table 1 at $j = 0.6$. The reaction front is located at $\zeta = 0$, where the rate of conversion is at maximum. The concentration of species from top to bottom at $\zeta = -10$: C^+, B, D^{2-}, K^+, and A^-

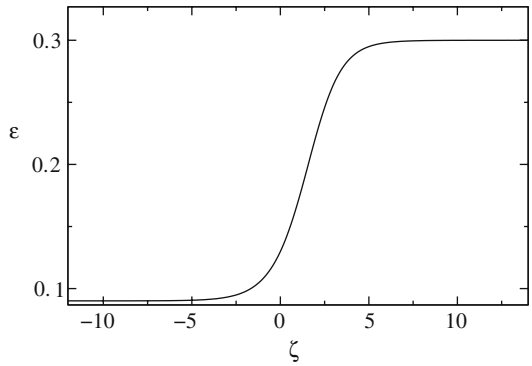

Fig. 2 Variation of electric field strength $\varepsilon = -\mathrm{d}\psi/\mathrm{d}\zeta$ across the front in Fig. 1

concentration level at 1.48, while the negatively charged D migrates backward yielding a smaller increase in its concentration (1.11).

The resultant electric field, presented in Fig. 2, reveals the common feature of the selected models; not only a liquid junction potential exists at the reaction front but also a significantly greater field strength is necessary ahead of the front in order to maintain the constant current density because the specific conductance of the system increases in the course of the reaction.

A positive electric field creates migrational fluxes that increase the overlap of reactant A and autocatalyst B at the reaction zone for the investigated systems with the exception of model 4 in Table 1. The resultant enhanced local rate of reaction in turn leads to an increased velocity of front propagation (cf. Eq. 9). In the opposite orientation the migrational fluxes point away from the reaction zone, decreasing the overlap of the reacting components leading to smaller velocity of front propagation as shown in Fig. 3. There also exists a current-density limit beyond which no reaction front can be sustained and the systems evolve into electrophoretic fronts propagating independently of each other. In model 4 both reactant A and autocatalyst B—having the same charge—migrate backward under a positive electric field, in which case a small increase in overlap may be observed as the reactant has a greater drift velocity due to the stronger electric field residing ahead of the front. In a negative field, although there is a decrease in the local reaction rate, the velocity of propagation increases because both A and B migrate forward. The former has greater drift velocity, so that reaction fronts are expected to extinguish at a strong negative field.

The investigated planar reaction fronts are stable in the absence of an electric field. In a positive field the greater migrational flux of reactant A with respect to that of autocatalyst B destabilizes the planar symmetry of the front and the amplification of the random noise leads to the formation of cellular structures as shown in Fig. 4. This loss of stability is not observed in model 5, indicating that higher-order autocatalysis—yielding a pushed front [4]—is a necessary condition for lateral instability similar to the diffusion-driven case. Planar fronts of model 4 in Table 1 also remain stable in the feasible range of current densities, whence a charge difference between the reactant and the autocatalyst is also essential to build up the necessary difference in migrational flux at the reaction zone.

The extent of instability is best characterized with the variation of the dispersion curve as the current density is increased for a positive electric field. Figure 5 depicts example cases for model 1. All wavenumbers have a negative growth-rate coefficient for $j = 0$ and $j = 0.2$, indicating that planar fronts are stable, while for the rest of the current densities planar fronts are unstable because a range of wavenumbers with a positive growth-rate coefficient appears. The wavenumber of the most unstable mode and the marginal wavenumber separating the stable and unstable regimes both increase upon increasing the current density.

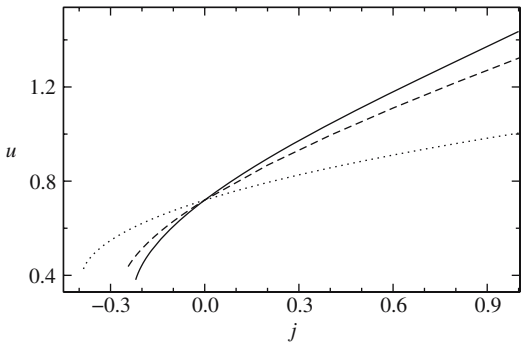

Fig. 3 Velocity of propagation of calculated planar fronts as a function of current density for models 1, 2, and 3 in Table 1

Fig. 4 Gray scale representation of a calculated front at $\tau = 140$ for model 1 in positive field with current density $j = 5$. The light region corresponds to low, the dark region to high concentration of autocatalyst B

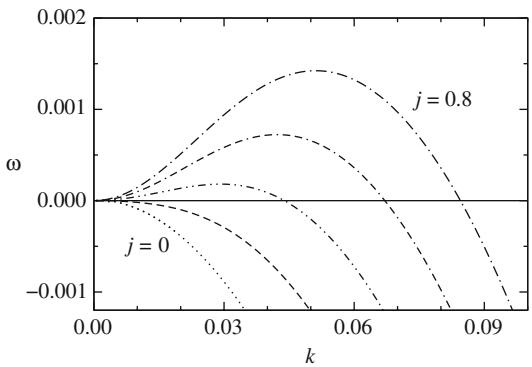

Fig. 5 Dispersion curves of planar fronts in model 1 calculated for current densities $j = 0.0, 0.2, 0.4, 0.6, 0.8$

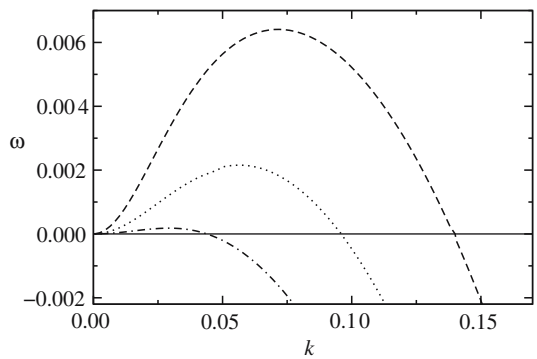

Fig. 6 Dispersion curves of planar fronts at current density $j = 0.4$ in models 1, 2, and 3 from bottom to top

Figure 6 illustrates that the degree of instability varies from system to system for a given current density. The unstable region and the growth-rate coefficient of the most unstable mode increase as the charge difference between autocatalyst B and reactant A increases. This effect is reflected in the current densities at the onset of instability, as shown in Table 2, where the slope of the dispersion curves—more precisely $\mathrm{d}\omega/\mathrm{d}(k^2)$—changes its sign at the origin. In models 1 and 2 the specific conductance of the product solution is three times that of the reactant solution in the absence of external electric field. This ratio changes only slightly upon introducing the field; hence an approximately three times stronger electric field is created ahead of the reaction front (cf. Eq. 5). In model 2 the onset of instability occurs at about half the current density with respect to model 1 because in the former the charge difference between the reactant and the autocatalyst is double. In model 3 planar fronts lose stability at even smaller current density because not only the charge difference between the key components increases further but also the product solution has a five times greater specific conductance with respect to the reactant solution resulting in a five times stronger field ahead of the front. Hence the ratio of specific conductance and the charge difference together determine the onset of instability, which may be estimated for the investigated models as

$$j_{cr} \approx \frac{\mathcal{C}}{(z_B - z_A)\kappa_{-\infty}/\kappa_{\infty}}, \tag{23}$$

where $\mathcal{C} = 0.9 \pm 0.1$.

Table 2 Critical current density at the onset of lateral instability

Model	1	2	3
j_{cr}	0.324	0.163	0.056

Although we have worked with only a few models, the results allow us to identify the possibility of lateral instability in further autocatalytic systems by considering the change in specific conductance during the reaction and the charges of the key components. Since the enhanced migration of the reactant with respect to that of the autocatalyst is the driving force, the electric-field strength has to be greater on the reactant side of the reaction front requiring an increase in specific conductance in the course of the reaction. The orientation of the electric field will depend on the charges of the species. Best results with relatively small current density are expected for systems in which the reactant(s) and the autocatalyst have opposite charges.

6 Conclusion

In this theoretical work we have investigated the interaction between ionic migration caused by an imposed electric potential gradient and a planar reaction front. For a model system, cubic autocatalysis between charged species is selected, while the external electric field is applied parallel to the direction of front propagation. In cubic autocatalysis the positive feedback is sufficiently strong so that the reaction front is a thin layer where the reactants are converted into the products, the stability of which is determined by the flux of the key species. Cellular fronts arise when the flux of the reactant through the reaction front significantly exceeds that of the autocatalyst, in which case transverse waves in the reaction front profiles develop from the microscopic noise in the system. When diffusion is the key transport process, the phenomenon is labeled diffusion-driven instability. For reacting components with different charges, the external electric field parallel to the direction of propagation leads to an additional flux of species due to ionic migration, which not only alters the velocity of front propagation but also may cause the planar reaction fronts to become unstable. The results of this work reveal that the onset of instability depends both on the charge difference between the reacting species and on the increase of specific conductance in the course of the reaction. The latter is an important characteristic of the front, since it is responsible for the stronger electric field ahead of the reaction front which selectively increases the flux of the reactant with respect to that of the autocatalyst, thus leading to the destabilization of the planar symmetry.

The reacting species in this study have equal diffusion coefficients rendering the resultant reaction fronts diffusively stable. In systems where the charged species diffuse at a different rate, a local electric field builds up in regions where concentration gradients exist. Migrational flux therefore contributes to mass transport in general systems, not only in the special case when an external electric field is applied. Hence a proper description of diffusion-driven front instability accompanying an autocatalytic reaction between charged species has to include migrational fluxes resulting from the local electric field at the front.

Acknowledgements This work was supported by the Hungarian Scientific Research Fund (OTKA T046010).

References

1. Epstein IR, Pojman JA (1998) Waves and patterns. In: An introduction to nonlinear dynamics: oscillations, waves, patterns, and chaos. Oxford University Press, Oxford, pp 109–138
2. Epstein IR, Showalter K (1996) Nonlinear chemical dynamics: oscillations, patterns, and chaos. J Phys Chem 100:13132–13147

3. Kuramoto Y (1980) Diffusion-induced chemical turbulence. In: Haken H (ed) Dynamics of synergetic systems. Proceedings of the international symposium on synergetics, Fed. Rep. of Germany, September 24–29, 1979. Springer, Berlin, pp 134–146
4. van Saarloos W (2003) Front propagation into unstable states. Phys Rep 386:29–222
5. Sivashinsky GI (1977) Diffusion-thermal theory of cellular flames. Comb Sci Technol 15:137–146
6. Horváth D, Petrov V, Scott SK, Showalter K (1993) Instabilities in propagating reaction-diffusion fronts. J Chem Phys 98:6332–6343
7. Malevanets A, Careta A, Kapral R (1995) Biscale chaos in propagating fronts. Phys Rev E 52:4724–4735
8. Merkin JH, Kiss IZ (2005) Dispersion curves in the diffusional instability of autocatalytic reaction fronts. Phys Rev E 72:026219
9. Horváth D, Showalter K (1995) Instabilities in propagating reaction-diffusion fronts of the iodate-arsenous acid reaction. J Chem Phys 102:2471–2478
10. Horváth D, Tóth Á (1998) Diffusion-driven front instabilities in the chlorite–tetrathionate reaction. J Chem Phys 108:1447–1451
11. Davies PW, Blanchedeau P, Dulos E, De Kepper P (1998) Dividing blobs, chemical flowers, and patterned islands in a reaction-diffusion system. J Phys Chem A 102:8236–8244
12. Fuentes M, Kuperman MN, De Kepper P (2001) Propagation and interaction of cellular fronts in a closed system. J Phys Chem A 105:6769–6774
13. Jakab É, Horváth D, Tóth Á, Merkin JH, Scott SK (2001) The effect of reversible binding of the autocatalyst on the lateral instability of reaction fronts. Chem Phys Lett 342:317–322
14. Tóth Á, Horváth D, Jakab É, Merkin JH, Scott SK (2001) Lateral instabilities in cubic autocatalytic reaction fronts: the effect of autocatalyst decay. J Chem Phys 114:9947–9952
15. Merkin JH, Ševčíková H (1999) Reaction fronts in an ionic autocatalytic system with an applied electric field. J Math Chem 25:111–132
16. Horváth D, Tóth Á, Yoshikawa K (1999) Electric field induced lateral instability in a simple autocatalytic front. J Chem Phys 111:10–13
17. Virányi Z, Szommer A, Tóth Á, Horváth D (2004) Lateral instability controlled by constant electric field in an acid-catalyzed reaction. Phys Chem Chem Phys 9:3396–3401
18. Virányi Z, Tóth Á, Horváth D (2005) Lateral instability induced by an inhomogeneous electric field. Chem Phys Lett 401:575–578
19. Virányi Z, Horváth D, Tóth Á (2006) Migration-driven instability in the chlorite–tetrathionate reaction. J Phys Chem A 110:3614–3618
20. Cohen SD, Hindmarsh AC (1996) CVODE, a stiff/nonstiff ODE solver in C. Comput Phys 10:138–143
21. Anderson E et al (1999) LAPACK users' guide Soc for Industrial and Applied Mathematics, Philadelphia